

Full length article

Segregation assisted grain boundary precipitation in a model Al-Zn-Mg-Cu alloy

Huan Zhao^a, Frédéric De Geuser^b, Alisson Kwiatkowski da Silva^a,
Agnieszka Szczepaniak^a, Baptiste Gault^{a,*}, Dirk Ponge^{a,**}, Dierk Raabe^{a,***}

^a Max-Planck-Institut für Eisenforschung, Max-Planck-Str. 1, 40237 Düsseldorf, Germany

^b Univ. Grenoble Alpes, CNRS, Grenoble INP, SIMaP, F-38000 Grenoble, France

ARTICLE INFO

Article history:

Received 5 May 2018

Received in revised form

28 June 2018

Accepted 1 July 2018

Available online 3 July 2018

Keywords:

Al-Zn-Mg-(Cu) alloy

Atom probe tomography

Grain-boundary segregation

Grain-boundary precipitation

Precipitate-free zones

ABSTRACT

Understanding the composition evolution of grain boundaries and grain boundary precipitation at near-atomic scale in aluminum alloys is crucial to tailor mechanical properties and to increase resistance to corrosion and stress corrosion cracking. Here, we elucidate the sequence of precipitation on grain boundaries in comparison to the bulk in a model Al-Zn-Mg-Cu alloy. We investigate the material from the solution heat treated state (475 °C), through the very early stages of aging to the peak aged state at 120 °C and further into the overaged regime at 180 °C. The process starts with solute enrichment on grain boundaries due to equilibrium segregation accompanied by solute depletion in their vicinity, the formation of Guinier–Preston (GP) zones in the solute-enriched grain boundary regions, and GP zones growth and transformation. The equilibrium segregation of solutes to grain boundaries during aging accelerates this sequence compared to the bulk. Analysis of the ~10 nm wide precipitate-free zones (PFZs) adjacent to the solute-enriched grain boundaries shows that the depletion zones are determined by (i) interface equilibrium segregation; (ii) formation and coarsening of the grain boundary precipitates and (iii) the diffusion range of solutes in the matrix. In addition, we quantify the difference in kinetics between grain boundary and bulk precipitation. The precipitation kinetics, as observed in terms of volume fraction, average radius, and number density, is almost identical next to the depletion zone in the bulk and far inside the bulk grain remote from any grain boundary influence. This observation shows that the region influenced by the grain boundaries does not extend beyond the PFZs.

© 2018 Acta Materialia Inc. Published by Elsevier Ltd. All rights reserved.

1. Introduction

Grain boundaries differ in structure and properties from the grain interiors. These differences cause chemical partitioning phenomena between the two regions. Specific solutes segregate to grain boundaries, driven by the Gibbs adsorption isotherm, an effect which modifies the grain boundary composition compared to the bulk. Such equilibrium segregation phenomena play an important role for transport and phase transformations [1–5], as well as for the material's strength and strain hardening [6], mechanical creep [7], liquid metal embrittlement [8,9] and corrosion

behavior [10]. Several thorough investigations of solute decoration behavior at grain boundaries at the near-atomic scale have been reported e.g. for Fe alloys [11–15]. Detailed segregation studies were also published on ultrafine grained Al alloys [16–20], yet, better general understanding of grain boundary segregation in conventional coarse-grained Al alloys is required, particularly in high-strength Al-alloys with multiple substitutional elements. Here we address this topic for a model Al-Zn-Mg-Cu alloy, representing the essential engineering class of 7xxx ultrahigh strength Al alloys. In these materials grain boundary segregation plays an essential role for several reasons: First, they are well known to become highly susceptible to stress corrosion cracking and subject to brittle intergranular fracture under certain conditions of heat treatment [21–24]. The embrittlement has been attributed to the formation of coarse, incoherent precipitates along grain boundaries, which leads to softening and substantially reduces the fracture resistance of these materials [25–27]. Second, interfacial segregation in these

* Corresponding author.

** Corresponding author.

*** Corresponding author.

E-mail addresses: b.gault@mpie.de (B. Gault), d.ponge@mpie.de (D. Ponge), d.raabe@mpie.de (D. Raabe).

alloys is generally associated with the formation of ~100 nm wide precipitate-free zones (PFZs) as the grain boundaries trap the solutes located adjacent to them [28,29]. This well-known phenomenon is characterized by strong elemental partitioning among the solute-enriched grain boundaries, the depleted regions adjacent to them and the unaffected grain interiors [30]. Similar aspects apply to the quenched-in vacancies to which the interfaces and precipitates can act as sinks [31,32]. This spatially highly confined compositional variation at and around grain boundaries, which is essentially driven by the Gibbs adsorption isotherm, creates very high local electrochemical and mechanical contrast, often reducing the alloy's corrosion resistance and mechanical properties [33–35]. Both phenomena are essential as further tuning of high strength Al alloys as key materials for light-weight transportation solutions is limited more by the weakness of the internal interfaces rather than by insufficient strength of the grain interiors.

The precipitation sequence in the bulk of Al-Zn-Mg-Cu alloys has been studied by several groups and is well understood [36–43] in terms of the individual processes of solid solution \rightarrow GP zones \rightarrow metastable $\eta' \rightarrow$ stable η (MgZn_2). In addition, the final structure of grain boundary precipitates has been studied [44–46]. Most of the grain boundary dependent phenomena discussed in these works refer to changes in kinetics, i.e. the precipitation and coarsening phenomena observed are generally faster on the interfaces than in the bulk grains. Yet, it must also be considered that equilibrium grain boundary segregation creates locally a different composition, characterized by higher and/or different solute content than in the grain interior. Segregation changes the local thermodynamic state at grain boundaries in a sense that it can in principle influence the sequence, composition and type of the precipitates that are formed. However, details regarding segregation, the evolution of grain boundary chemistry, the early stages of grain boundary precipitation and the formation of the PFZs in Al-Zn-Mg-Cu alloys are lacking. These knowledge gaps hinder precise understanding of the interplay between decoration, formation, growth, and kinetics of grain boundary precipitation, and hence prevent tailoring grain boundaries and avoiding the adjacent precipitation free regions for the design of materials with better mechanical and corrosion properties.

Atom probe tomography (APT) provides three-dimensional (3D), near-atomic scale analytical mapping of materials, and is uniquely positioned to measure the local chemical composition and 3D morphology of individual grain boundary and precipitates [47–51]. More intense deployment of its capabilities to investigate grain boundaries in Al-based alloys has been hindered by the lack of reliable methods to prepare site-specific specimens, i.e. APT tips containing specific features such as grain boundaries. Most APT specimens in this field have so far been prepared with the aid of a focused-ion-beam (FIB) that makes use of a Ga source. Ga implantation however causes sample embrittlement in Al-alloys [52,53], as it gets readily trapped at interfaces, dislocations and grain boundaries. Also it can promote formation of a low-melting Al-Ga eutectic [54]. The recent development of an alternative ion source for FIBs, based on a Xe plasma, has thus been used in the current study to alleviate this stringent limitation [55].

The objective of the present work is to investigate grain boundary precipitation in comparison to bulk precipitation, from the solution heat treated state (475 °C), through the very early stage of aging (120 °C/0.5 h), peak aged state (120 °C/24 h) and further into the overaged regime (120 °C/24 h + 180 °C/6 h). In that context we also followed the kinetics of partitioning of the solutes from the matrix to the interfaces, the formation and growth of the precipitates in the bulk and at the grain boundaries, solute segregation to grain boundaries and the evolution of PFZs, so as to unveil the effects of segregation on grain boundary precipitation in a model

Al-Zn-Mg-Cu alloy in a more holistic fashion. We made use of a parameter-free methodology introduced in Ref. [56], to efficiently extract information from APT data such as matrix and precipitate composition, volume fraction, and number density. APT is combined with transmission electron microscopy (TEM), electron backscattered diffraction (EBSD) characterization and hardness measurements to study the effects of segregation on grain boundary precipitation in a model Al-Zn-Mg-Cu alloy.

2. Materials and methods

The alloy used in this investigation is a model Al-Zn-Mg-Cu alloy. It was laboratory-cast in a vacuum induction furnace to a rectangular ingot with dimensions of 200 mm \times 190 mm \times 40 mm. The ingot was homogenized in an Ar-atmosphere furnace for 1.5 h at 475 °C and subsequently water quenched. The homogenized ingot was then subsequently hot-rolled from 40 mm down to a 3 mm thick sheet at 450 °C and finally solution heat treated for 1 h at 475 °C and then water quenched. The quenched material was immediately aged at 120 °C for different times and subsequently water quenched to room temperature. The aging times were 0.5 h, 2 h and 24 h. Aging at 120 °C for 24 h produces the peak aged state. The peak aged sample was further aged for 6 h at a higher temperature of 180 °C to obtain overaged material. The different aging times were selected in order to follow the kinetics of precipitation according to the hardness curve, which can be found in Ref. [56]. Table 1 summarizes the chemical composition of the homogenized ingot measured by wet chemical analysis. Zr was added to the alloy to produce Al_3Zr dispersoids, which refine the grain size.

APT specimens were prepared to investigate the precipitation at the grain boundaries. EBSD was first used to locate high-angle grain boundaries. APT specimens were then prepared from such regions by site-specific preparation as outlined in Ref. [57] on a FEI Helios Plasma focused ion beam (PFIB) using of a Xe source on commercial silicon micro-tip coupons (Cameca Inc.) as support. Specimens were sharpened by using a 30 kV Xe^+ ion beam, followed by a 5 kV final cleaning step to remove regions with higher concentrations of implanted high-energy Xe^+ ions. APT analyses were performed on a Cameca Instrument Inc. Local Electrode Atom Probe (LEAP) 5000XS (straight flight path). The detection efficiency of this instrument is approx. 80% owing to the improved multi-channel plate detector equipped with a fine hole-array. The measurements were performed at a base temperature of 50 K in voltage-pulsed mode. The pulse fraction, pulse rate and target detection rate of the measurement were 20%, 250 kHz and 1%, respectively. Datasets containing 70–150 million ions were acquired for each aging state. APT reconstruction and analysis were carried out using the Integrated Visualization and Analysis software (IVAS). The reconstruction parameters were calibrated according to the partial structural information within the dataset following the protocol described by Gault et al. [58]. TEM observations were performed on a JEOL JEM-2200 FS, operated at 200 kV conducted on a PFIB-prepared sample.

3. Results

A typical APT dataset of the Al-Zn-Mg-Cu alloy containing a grain boundary in the as-quenched state is shown in Fig. 1. The EBSD map shows the high angle grain boundary where several APT

Table 1

Bulk chemical composition of a model Al-Zn-Mg-Cu alloy obtained from wet chemical analysis.

Alloy	Zn	Mg	Cu	Zr	Fe	Si	Al
(wt %)	6.22	2.46	2.13	0.155	0.021	<0.01	Rest

samples were prepared from in the as-quenched state. Fig. 1(b) displays a 2D desorption map directly extracted from the APT dataset. The {111} poles of the top and bottom grains are indexed, indicated by dashed circles.

The grain boundary is highlighted in the 3D atom map in Fig. 1(c) in terms of the region enriched in Zn, Mg, and Cu. The observation reveals that all solute elements segregate to the grain boundary already during quenching. Fig. 1(d) shows the mean chemical composition across the grain boundary. Each data point of the composition profile represents the number of atoms of a specific species relative to all other species identified, and the error bar represents the standard deviation (2σ) on each of the values. The analysis reveals 4.6 at% Zn, 4.5 at% Mg, and 1.6 at% Cu enrichment, corresponding to a grain boundary compositional excess (multiplier factor) of about 2 for Zn, 2 for Mg and 3 for Cu relative to the adjacent bulk solute composition. It should be noted that in the as-quenched state, the size and chemical contrast of the clusters/GP zones do not allow for a straightforward visualization by iso-composition surfaces.

Fig. 2 shows the APT analysis after aging for 0.5 h at 120 °C. Nano-sized precipitates are visible in the alloy, highlighted by 6 at% Zn iso-composition surfaces. The grain boundary is observed edge-on, shown by the precipitate enriched region as indicated by the red arrow in Fig. 2(a). Spherical precipitates enriched in Zn and Mg are clearly revealed within the grain boundary in Fig. 2(b). The composition profile across one grain boundary precipitate shows that it contains 60 at% Al, 20 at% Zn, 18 at% Mg and 2 at% Cu. These values are close to the composition expected for GP zones (Al_2ZnMgCu) as reported in the literature [37,59–63]. The GP zones distributed within the grain boundary are around 5 nm in size, i.e.

larger than the zones with 3 nm in size formed in the adjacent bulk region.

Typical precipitate-free zones concurrently form adjacent to the grain boundary when the GP zones become visible, as indicated by the purple dashed lines in Fig. 2(a). The uniformity of the PFZs indicates a recrystallized microstructure [64]. A corresponding composition profile taken across the grain boundary in Fig. 2(d) reveals that the content of Zn and Mg is about 1.5 at% in the PFZs and is lower than inside the grain interior far away from the interface. This observation indicates that we do not only observe precipitate formation on the grain boundary but also solute depletion in the PFZs.

The precipitation behavior after aging at 120 °C for 2 h is shown in Fig. 3(a) with the grain boundary highlighted by a red rectangle. The grain boundary precipitates assume a rod-like morphology as shown in Fig. 3(b), which contrasts with the near-spherical GP zones formed in the abutting bulk. The corresponding composition with one grain boundary precipitate shows that it consists of about 61 at% Al, 21 at% Zn, 15 at% Mg and 3 at% Cu. This observation suggests that these precipitates are probably still GP zones, despite their change in morphology.

Fig. 4 shows the result of the APT analysis of the specimen in peak aged state, i.e. after 24 h at 120 °C. A high number density ($1 \times 10^{24} \text{ m}^{-3}$) of small precipitates is homogeneously distributed in the bulk. In Fig. 4(b), a close-up image of one precipitate in the bulk near the {111} planes of the Al matrix shows that its morphology is near-spherical with a diameter of around 7 nm. The corresponding composition presented in Fig. 4(c) indicates that these bulk precipitates are mainly GP zones, which profoundly contribute to strengthening.

Fig. 4(d) shows that a few isolated large precipitates formed along the grain boundary. Most of the grain boundary precipitates grow as thick plates and are larger than 20 nm in length. The compositional evolution is accompanied by this morphology change. The grain boundary precipitates contain less Al (25 at%) and more Zn (40 at%), i.e. their composition is close to that of $\text{Mg}(\text{Al}, \text{Zn}, \text{Cu})_2$, a stoichiometry which has been described as η' phase in previous studies [37,38,65]. We assume that within the grain boundary, there is a transition of GP zones into η' plates, while in the adjacent bulk grain the GP zones prevail. As η' and η might have similar chemical composition, due to Al substitution in the precipitates, we refer to these particles hereafter simply as η' instead of making a detailed distinction between η' and η . The large η' precipitates nucleate and grow on the grain boundary through the accumulation and merging of GP zones, as they have a much lower number density (10^{15} m^{-2}) compared to the initial stage of aging (10^{16} m^{-2}).

The precipitate-free zones shown in Fig. 4(a) are still noticeable in the peak aged state. In addition to the APT analysis, TEM was used to map the nanostructure in the vicinity of the grain boundary. The electron micrograph in Fig. 4(f) agrees well with the APT result in Fig. 4(a) and shows a comparable size of the coarse precipitates and the PFZs.

In the overaged state, one single large precipitate (~40 nm in length) is observed along the grain boundary as shown in Fig. 5(a). Some of the bulk precipitates show morphology changes which are characterized by a transition from the small spherical shape in the earlier stage towards coarse denser plates after aging. The chemical composition of the coarse precipitates from the bulk show less Al (~30 at%) compared to 60 at% Al in the precipitates in the peak aged state, suggesting that they are η' . These observations indicate that in the overaged state, some of the bulk precipitates transform from GP zones into η' precipitates. This finding is in contrast to the same phase transition that was observed for the grain boundary precipitates already in the peak aged state.

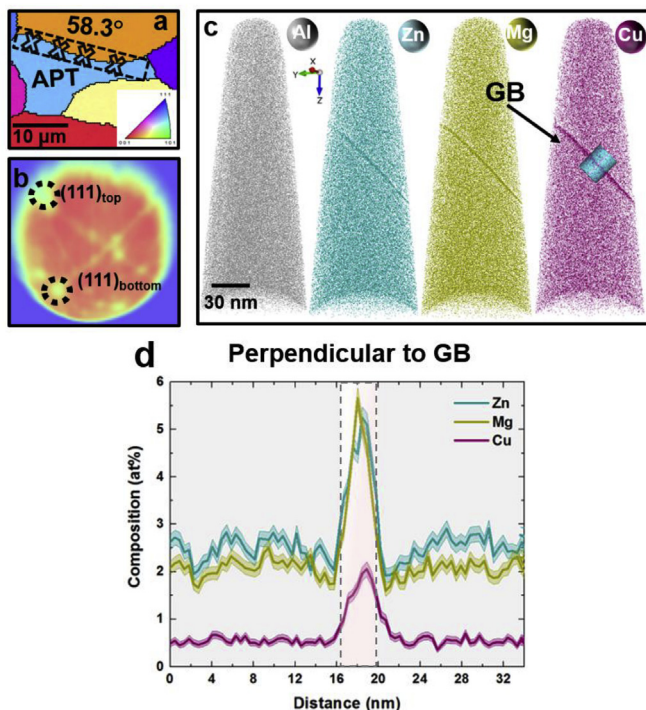


Fig. 1. Atom probe tomography analysis for a sample in the as-quenched state: (a) EBSD IPF map showing the grain boundary (GB) chosen for site-specific APT tip preparation; (b) Desorption map showing indexed crystallographic poles of two adjacent grains; (c) Atom maps of all elements in the as-quenched state; (d) Composition profile across the grain boundary in a 20 nm-diameter cylinder, taken along the z direction. (Al, Zn, Mg, and Cu are depicted in grey, dark cyan, olive, and dark red, respectively.). (For interpretation of the references to colour in this figure legend, the reader is referred to the Web version of this article.)

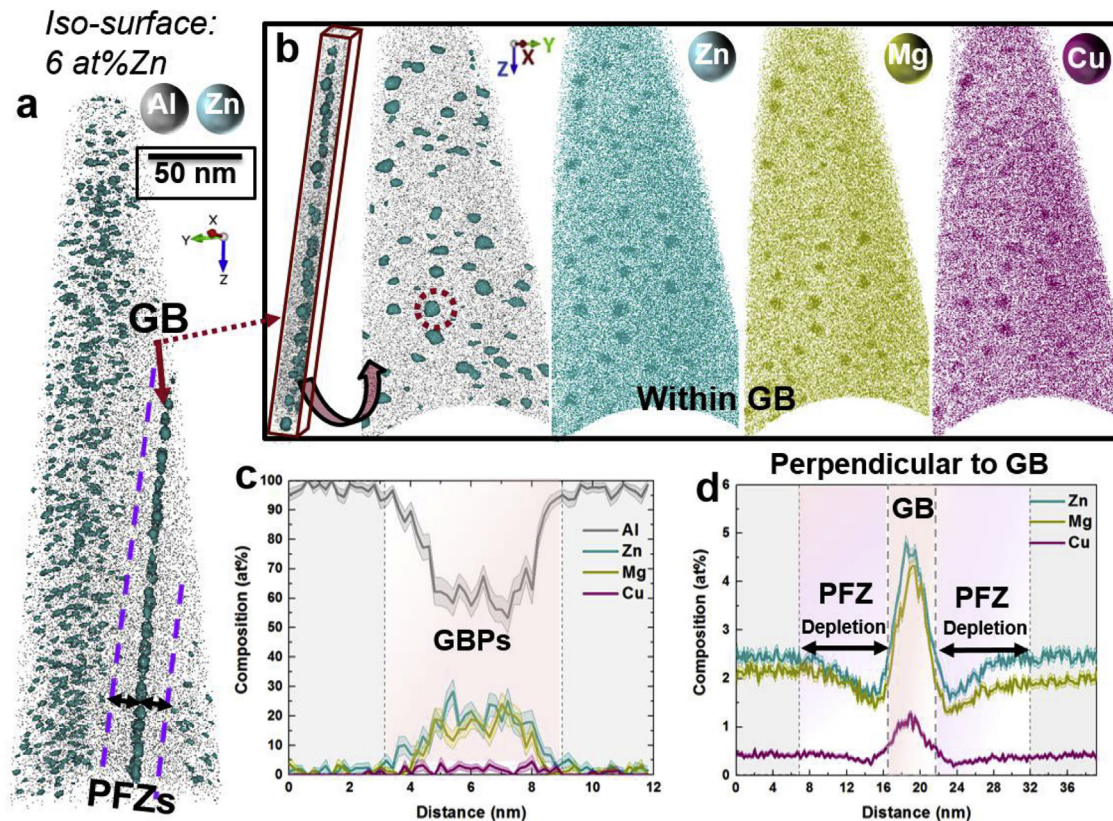


Fig. 2. Atom probe tomography analysis after aging for 0.5 h at 120 °C. (a) Precipitates visualized by adding iso-composition surfaces of 6 at% Zn; (b) Distribution of solutes within the grain boundary (of the region shown in **a** as indicated by the red arrow); (c) 1D composition profile showing the composition of the selected grain boundary precipitate (GBP) in a 5 nm-diameter cylinder along the z direction (of the region shown in **b** as indicated by dashed red circle); (d) 1D composition profile across the grain boundary, computed for a region between grain boundary precipitates, along a 25 nm-diameter cylindrical region-of-interest. (Al, Zn, Mg, and Cu are depicted in grey, dark cyan, olive, and dark red, respectively.). (For interpretation of the references to colour in this figure legend, the reader is referred to the Web version of this article.)

4. Discussion

4.1. Quantification of the precipitation reaction

We recently introduced a new methodology to process radial distribution function based model fitting from atom probe data to provide complete characterization of both the precipitates and the matrix, without the need for any input parameters [56]. The global composition of the entire datasets is derived from counting the relative number of ions of each element within the mass spectrum. The matrix composition is derived from the distribution of isolated atoms based on the probability for each solute to have no neighbor (i.e. to be isolated) at a given distance, in comparison to that obtained from a random distribution of solutes [66]. For characterizing the precipitates present in the volume, we use radial distribution functions calculated with each solute of a specific species as the central atom.

Here, this approach allows us to quantify the evolution of the precipitation sequence from three different regions, namely, bulk (far from the grain boundary), near grain boundary (region adjacent to the grain boundary), and directly on the grain boundary. The three different regions are depicted in Fig. 6, taking the peak aged state as an example. For evaluating the precipitation state in the bulk, we use the APT datasets obtained from the grain interiors as discussed in more detail in Ref. [56]. For regions near GBs and on GBs, we used cuboidal shaped regions-of-interest to split the tomographic reconstructions (shown in Figs. 1–5) into two subsets, i.e., one containing the grain boundary only and another one

containing the adjacent bulk after extraction of the grain boundary zone. The PFZs existing in the vicinity of the grain boundary are essentially included in the near-GB region. However, it must be considered that the PFZs and the grain boundaries in the APT reconstructions may vary in size by about 10% along the GB plane so that some of the analysis features can overlap.

Fig. 7(a) presents the evolution of the global and matrix composition values measured in the bulk and the near-GB region. In the near-GB region, the global composition of Zn decreases from 2.6 to 2.3 at% in the peak aged state and more significantly to 1.7 at% in the overaged state. The global composition of Mg in the near-GB region also drops from 2.2 to 1.7 at% in the overaged state. These findings are attributed to the depletion of solutes in the PFZs through segregation to the GB which is in diffusional reach. The observed increase in the solute composition after 0.5 h in the near-GB region, as indicated by dashed red circles, is likely related to artifacts in the investigated dataset that exhibits a large crystallographic pole. This effect is known to sometimes affect the distribution of solutes [67]. However, when excluding this questionable point, we clearly observe formation of precipitates through their consumption of solutes (global minus matrix) and we also find that the evolution of the matrix composition during aging is essentially similar in the bulk and in the near-GB regions.

Fig. 7(b) presents the evolution of the precipitates' composition during aging within all three zones, namely, the bulk, near-GB and on-GB. In the peak aged state, the precipitates' composition in the bulk and the near-GB regions are approx. 60 at% Al, 20 at% Zn, 18 at% Mg and 2 at% Cu, i.e. they match the composition of the GP zones

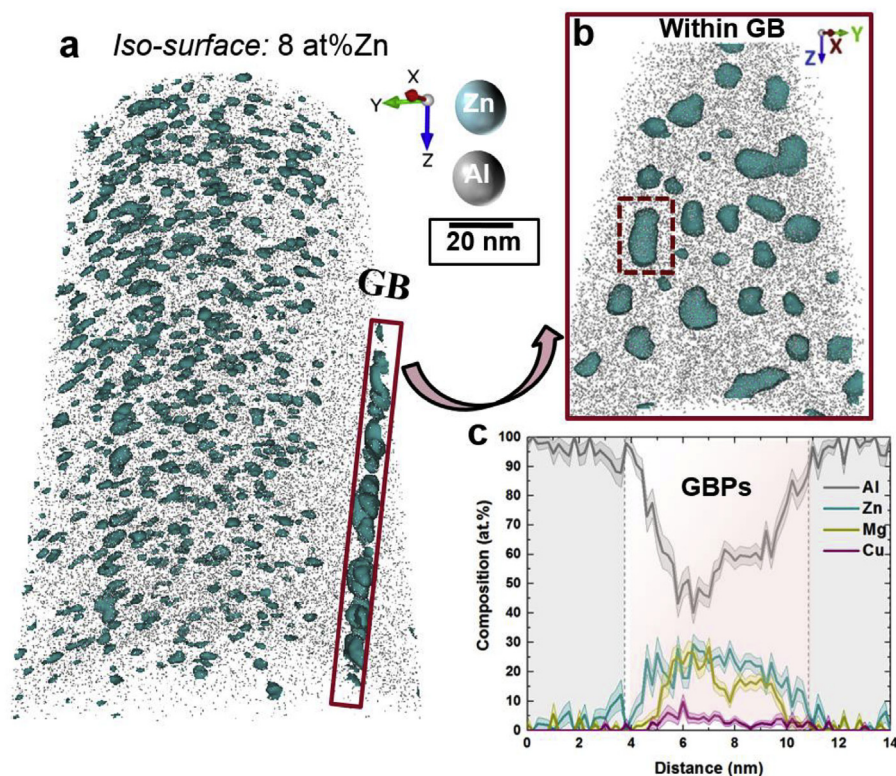


Fig. 3. Atom probe tomography analysis showing the nanostructure formed after aging for 2 h at 120 °C. (a) Precipitates are highlighted in terms of 8 at% Zn iso-composition surfaces; (b) Close-up map of the grain boundary precipitates (of the region shown in **a** as indicated by the solid red rectangle); (c) 1D composition profile showing the chemistry of the selected grain boundary precipitate, plotted along a 5 nm-diameter cylindrical region-of-interest (of the region shown in **b** as indicated by the dashed red rectangle). (Al and Zn are depicted in grey and dark cyan, respectively.). (For interpretation of the references to colour in this figure legend, the reader is referred to the Web version of this article.)

which prevail upon aging. Only when the specimen is overaged at 180 °C, the composition of the precipitates reaches a content which matches η' phase. This structural transition is associated with significant capillary driven competitive particle coarsening, which also leads to degradation of the mechanical properties [61]. The Cu content (2 at%) remains unchanged after long time aging at 120 °C, while it exhibits a strong increase to 5 at% in the overaged state both in the bulk and also in the near-GB region. This is explained by the low diffusivity of Cu, together with its solubility in the GP zones according to a previous study [68].

On the GB, the transition from spherical GP zones to plate-shaped η' phase occurs already in the peak aged state as revealed in Fig. 4 and shown in terms of the precipitates' composition in Fig. 7(b).

Fig. 8 shows the volume fraction, average radius, the number density of the precipitates, and the distance between them. Since the solute content of the precipitates evolves with aging, we chose to represent only the contribution of the solutes to the volume fraction to better visualize the progress of the reaction.

The results show that a large number density (10^{25} – 10^{26} m $^{-3}$) of very small (1 nm in size) solute-rich clusters has formed already in the as-quenched state in the three regions studied. This might be caused by the natural aging during sample preparation and by the fact that real sample quenching does actually happen over a non-zero time interval which leaves enough time for short relaxation diffusion.

Over the first 2 h at 120 °C aging, in the bulk and near-GB regions a high number density (10^{24} – 10^{25} m $^{-3}$) of nearly spherical zones enriched in Zn and Mg form and develop into GP zones. In the same time interval, the volume fraction of precipitates increases to 1% both in the bulk and near-GB zones, i.e. new precipitates formed

and coarsened. Significant coarsening occurs in the overaged state as revealed by the increase of precipitate radius, volume fraction, and inter-precipitate distance. Remarkably, the precipitation kinetics, as observed in terms of the fraction, average size, and number density, are almost identical in the bulk and near-GB regions. This finding confirms that the region of influence that acts on the grain boundary precipitation does not extend beyond the PFZs, i.e. typically 8–11 nm for the current material and aging states.

We also observe that in the initial stage of aging (0.5 h at 120 °C aging), the mean radius (~5 nm in size) of the clusters/GP zones on the GB is already larger compared to those in the bulk and near-GB regions (~3 nm in size). During long time aging, the precipitates that are located on the GB have a larger radius and interparticle spacing, and a lower number density.

4.2. Chemical composition on grain boundaries and within PFZs during aging

Direct analysis of the chemical composition on the grain boundaries provides additional information enabling better understanding of grain boundary segregation and precipitation. The global composition of the grain boundary regions and the available solute composition as a function of aging time were quantified separately. We analyzed the global grain boundary composition by taking the whole grain boundary volumes into account including the grain boundary precipitates. We also quantified the solute composition on the grain boundaries by measuring the average values over selected areas of the grain boundary devoid of precipitates. These were 20 nm-diameter cylindrical regions-of-interest taken across such grain boundary segments that did not include any precipitate.

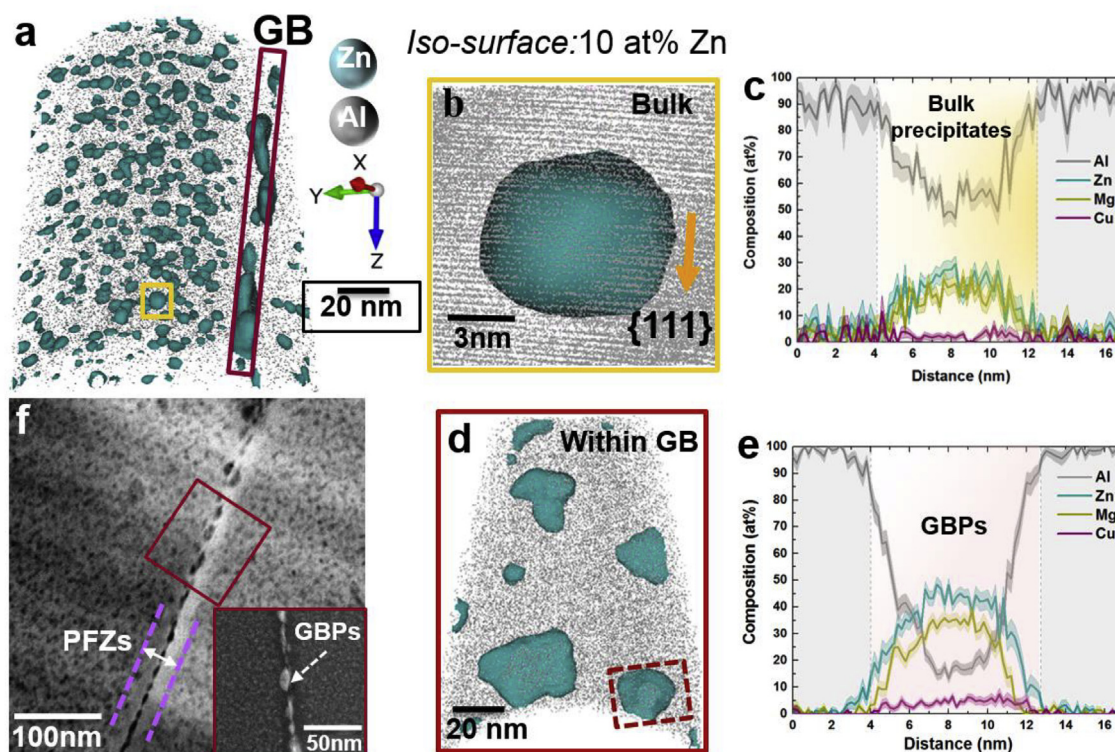


Fig. 4. Atom probe tomography analysis taken on a specimen after aging for 24 h at 120 °C. (a) Precipitates highlighted in terms of 10 at% Zn iso-composition surfaces. (b) Close-up image of one precipitate in the bulk, taken with a view along the {111} planes of the Al matrix (of the region in **a** indicated by the solid yellow rectangle); (c) 1D composition profile showing the chemistry of the selected bulk precipitate, plotted along a 5 nm-diameter cylindrical region-of-interest; (d) Image of the precipitates within the grain boundary (of the region shown in **a** as indicated by the solid red rectangle); (e) 1D composition profile showing the chemistry of the selected grain boundary precipitate, taken along a 10 nm-diameter cylindrical region-of-interest (of the region shown in **d** as indicated by dashed red rectangle); (f) Electron micrograph shows the comparable size of the precipitates and of the PFZs in the peak aged state. (Al and Zn are depicted in grey and dark cyan, respectively.). (For interpretation of the references to colour in this figure legend, the reader is referred to the Web version of this article.)

The global composition on the grain boundaries as shown in Fig. 9(a) is characterized by strong solute segregation to the grain boundary already after quenching with a grain boundary excess of about 2 for Zn, 2 for Mg and 3 for Cu relative to the solute composition in the bulk. The global composition on the grain boundaries increases due to inbound diffusion from the adjacent bulk during aging. The observed sharp increase in the global composition on the grain boundary in the overaged state as shown in Fig. 9(a) is most likely related to the single large precipitate imaged within the dataset. This can therefore be ascribed to the small volumes sampled by APT. The average solute content on the grain boundaries decreases during aging as shown in Fig. 9(b). More specifically, ~4.7 at% solute Zn in the as-quenched state decreases to ~1.2 at% in the overaged state and ~4.5 at% solute Mg in the as-quenched state decreases to ~1.8 at% in the overaged state on the grain boundaries. We take this observation as an indication for the diffusion of the segregated solutes also along the grain boundaries, contributing to the growth and coarsening of the grain boundary precipitates during aging.

The PFZs appear over the entire aging process as shown in Figs. 2–5. Each individual PFZ region was extracted from the APT reconstruction using cuboidal regions-of-interest. Fig. 9(c) shows the solute composition as averaged over the probed PFZs as a function of aging time. In the as-quenched state, the solute content in the PFZs is almost at the same level as in the grain interiors. The solute composition within the PFZs shows a sharp drop between 2 h and 24 h aging at 120 °C (Zn: from 1.8 to 0.5 at%; Mg: from 1.6 to 0.7 at%). The composition of Zn and Mg within the PFZs are lower than in the grain interiors at the same aging times as shown in

Fig. 7(a), e.g. by a depletion factor of 0.7 for Zn, 0.6 for Mg and 0.6 for Cu relative to the grain interior in the peak aged state. This finding indicates that the PFZs are not only devoid of any precipitates but are also solute depleted. This result is attributed to the formation and coarsening of grain boundary precipitates which are enriched in Zn and Mg, but also to the Gibbsian segregation of solutes to the boundaries which is driven by the reduction in grain boundary energy. The insufficient diffusion range of the available matrix solute content adjacent to the PFZs and the formation of precipitates in the matrix explain this sustained solute depletion in the PFZs. The solute composition within the PFZs shows a slight decrease by a factor of ~0.2 of Zn and Mg during the overaging step. This observation suggests that only a small amount of additional solutes segregate to the grain boundaries at the later stage of aging.

The variation in the PFZs width during aging is shown in Fig. 9(d). The PFZs width are measured from the grain boundaries to the edges of the PFZs when looking edge-on at the grain boundary. The PFZs width is around 11 nm at the initial state of aging (0.5 h at 120 °C), measured from the left purple line to the grain boundary as shown in Fig. 2(a). It becomes narrower after 2 h aging to a value of 8 nm and then remains almost constant during the later stages of aging. This result reveals that GP zones can still form in those regions of the PFZs close to the grain interiors from which solutes penetrate, driven by the composition gradient.

4.3. Grain boundary precipitation sequence and PFZ formation

Based on the APT results, our view of grain boundary precipitation and formation of PFZs is schematically shown in Fig. 10,

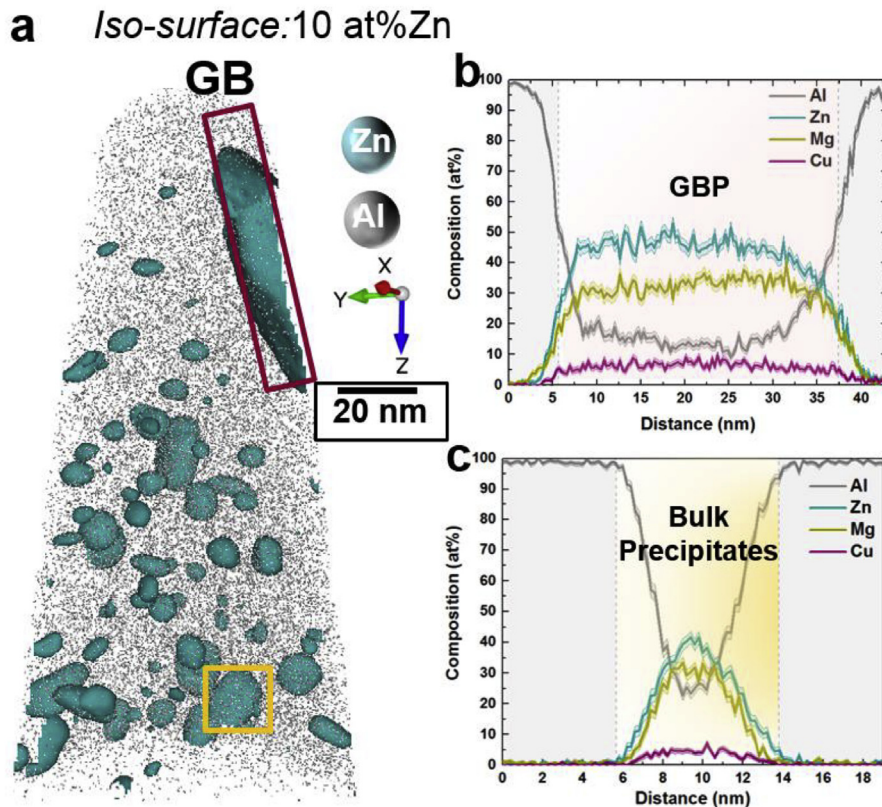


Fig. 5. Atom probe tomography analysis in the overaged state: (a) Precipitates highlighted in terms of 10 at% Zn iso-composition surfaces; (b) 1D composition profile showing the chemistry of the selected grain boundary precipitate (of the region shown in **a** as indicated by solid red rectangle); (c) 1D composition profile showing the chemical composition of the selected bulk precipitate (of the region shown in **a** as indicated by solid yellow rectangle). (Al and Zn are depicted in grey and dark cyan, respectively.). (For interpretation of the references to colour in this figure legend, the reader is referred to the Web version of this article.)

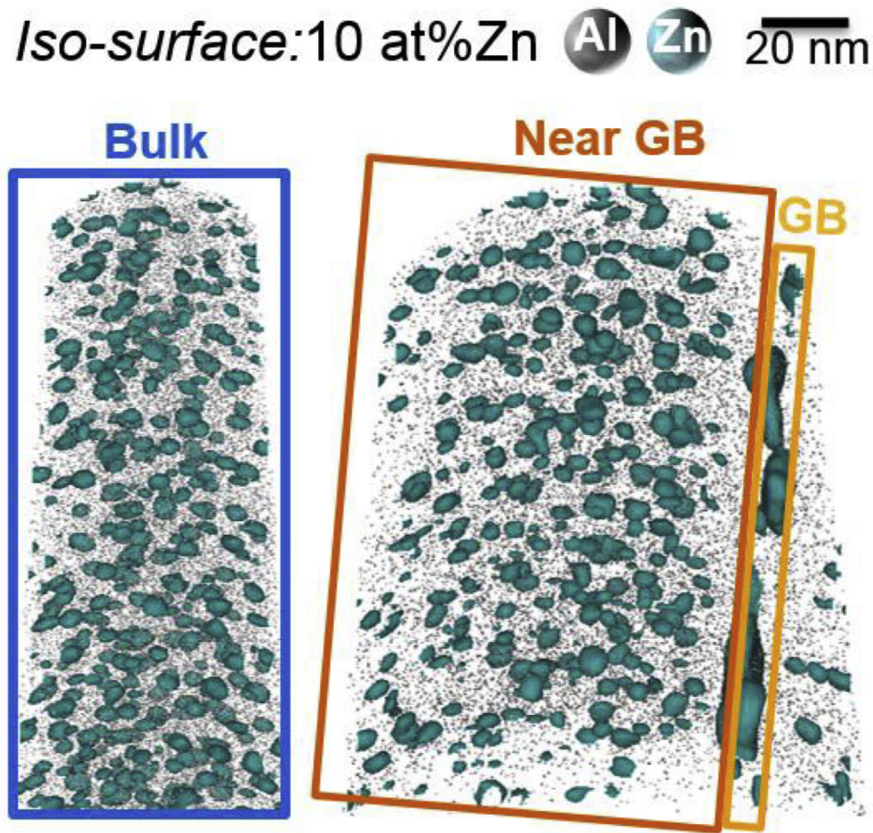
where solute atoms, nanoclusters, and precipitates are shown.

In the as-quenched state, before any GP zones become visible, solutes have already segregated to the grain boundaries with a grain boundary excess of about 2 for Zn, 2 for Mg, and 3 for Cu. Solute segregation to the grain boundaries is driven by the equilibrium adsorption isotherm described originally by Gibbs and later by McLean and others [5,69–71]. This means that the increased solute concentrations on the decorated grain boundaries are in local thermodynamic equilibrium with the lower concentrations in the adjacent bulk matrix, i.e. the solutes partition among grain boundaries and grain interiors. In the initial state of aging (0.5 h at 120 °C), the Gibbs-driven equilibrium grain boundary segregation leads to a locally higher composition of Zn and Mg, yet, at constant local chemical potential as schematically shown in Fig. 11. This local increase in solute concentration on the grain boundaries causes higher compositional levels and corresponding fluctuations along the grain boundaries and thus also earlier formation of GP zones compared to the grain interiors.

The GP zones distributed along the grain boundary are on average around 5 nm in size after 0.5 h at 120 °C, i.e. they are substantially larger than the GP zones with 3 nm in size formed in the bulk. The fast formation of GP zones on the grain boundary rapidly traps solutes, both from the interface itself but also from the region adjacent to it. These processes are kinetically supported by the highly abundant quenched-in vacancies which heal out rapidly, thereby providing additional solute transport. This local partitioning between the Gibbs-decorated grain boundary and the region adjacent to them reduces the remaining solute composition in the near-interfacial zones. This effect kinetically reduces the availability

of solutes in this region to a level insufficient to form precipitates, hence causing the formation of PFZs. This means that the first step in this process is determined by a local equilibrium mechanism, i.e. driven by the Gibbs isotherm decoration of the grain boundary by Zn, Mg and Cu. The second step is the spinodal decomposition of the segregated solutes into enriched and depleted grain boundary regions leading to the heterogeneous nucleation of precipitates [72]. The third step, namely, the solute depletion of the regions adjacent to the interface, is related to kinetics and governed by the mass transport of those solutes that are in reach for a given time and temperature so as to follow the Gibbs adsorption isotherm and the associated confined spinodal decomposition at interfaces [72]. As mentioned above the formation of these PFZs is further influenced by the fact that the grain boundaries act as vacancy sinks, an effect which further reduces kinetics in the PFZs as suggested by Nicholson et al. [28,31,73–75].

With aging time increasing (between 2 h and 24 h at 120 °C), solutes from the bulk keep segregating, forming a flux of solutes towards the grain boundaries. The growth and transformation of the GP zones on the grain boundaries are accelerated by the solute segregation from the matrix and enhanced solute diffusion along the grain boundaries. Solute segregation creates a gradient of composition from the bulk to the grain boundaries, also promoting the growth and coarsening of grain boundary precipitates. These effects result in precipitate growth and transformation into thick η' plates with 15 nm in average length on the grain boundaries in the peak aged state, while the bulk contains mainly spherical GP zones with an average size of only 4 nm. Upon long time aging, GP zones can still form within the PFZs close to the interior of the grains with



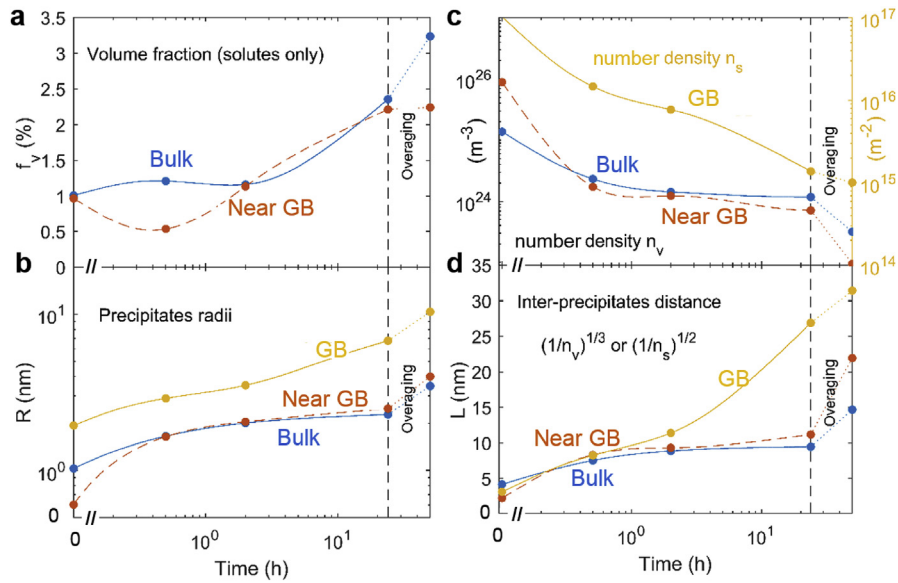


Fig. 8. Evolution of the precipitates during aging in terms of (a) Volume fraction; (b) Radius; (c) Number density per volume in the bulk and near-GB regions as shown on the left axis, and the precipitate number density per area on the GB as shown on the right axis; (d) Average distance between precipitates (The regions of interest, viz., the Bulk, Near-GB, and on -GB regions are depicted in blue, orange, and yellow, respectively.). (For interpretation of the references to colour in this figure legend, the reader is referred to the Web version of this article.)

a certain remaining supply of solutes. This effect reduces the width of the PFZs to 8 nm after long time aging compared to 11 nm observed in the initial state of aging.

During overaging (6 h at 180 °C after peak aged), some of the bulk precipitates transform to η' precipitates, resulting in a mixed distribution of GP zones and η' precipitates in the bulk. On the grain

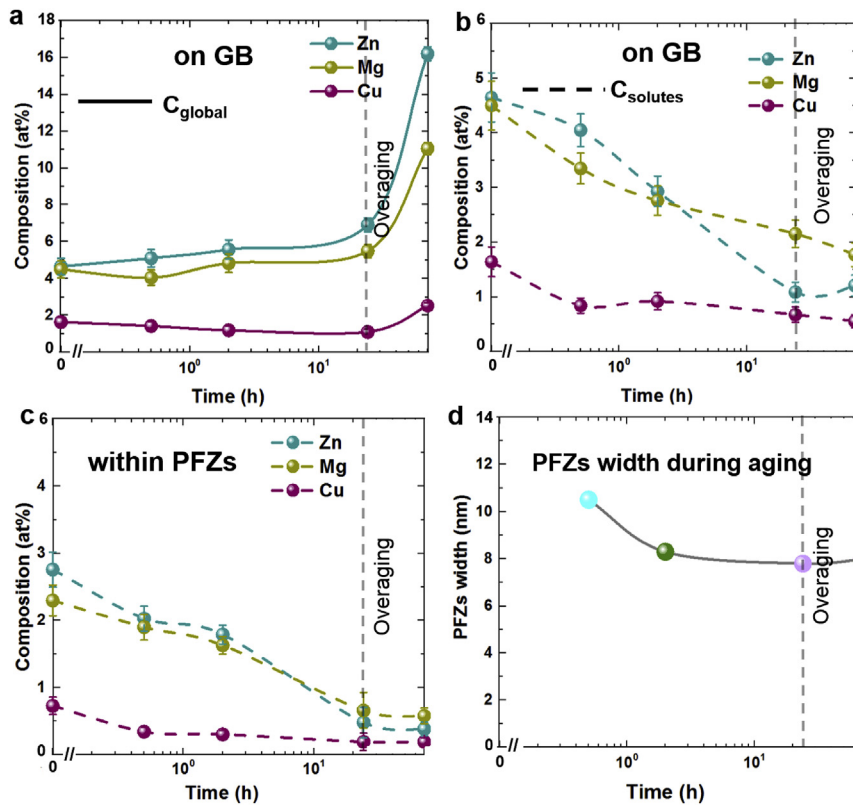


Fig. 9. Evolution of the grain boundary composition: (a) Global composition measured over the entire grain boundaries including the grain boundary precipitates; (b) Average solute composition on the grain boundaries, quantified by measuring the average values over selected areas of the grain boundary devoid of precipitates. These were 20 nm-diameter cylindrical regions-of-interest taken across such grain boundary segments that did not include any precipitate. (c) Solute composition within the PFZs; (d) Variation of the width of the PFZs during aging. (Zn, Mg, and Cu are depicted in dark cyan, olive, and dark red, respectively.). (For interpretation of the references to colour in this figure legend, the reader is referred to the Web version of this article.)

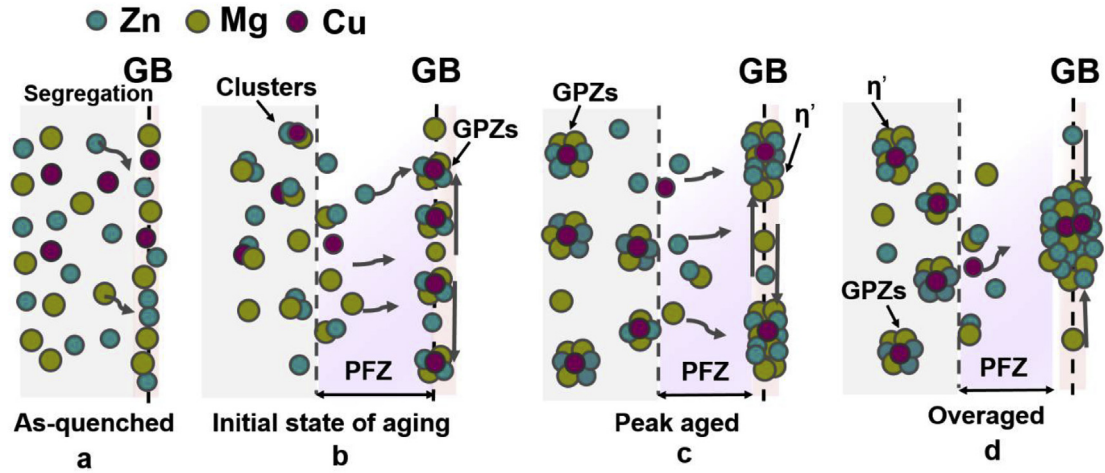


Fig. 10. Schematic diagrams of the grain boundary precipitation and PFZs formation during aging: (a) As-quenched state; (b) Initial state of aging (0.5 h at 120 °C); (c) Peak aged; (d) Overaged. (Zn, Mg, and Cu are depicted in dark cyan, olive, and dark red, respectively.)

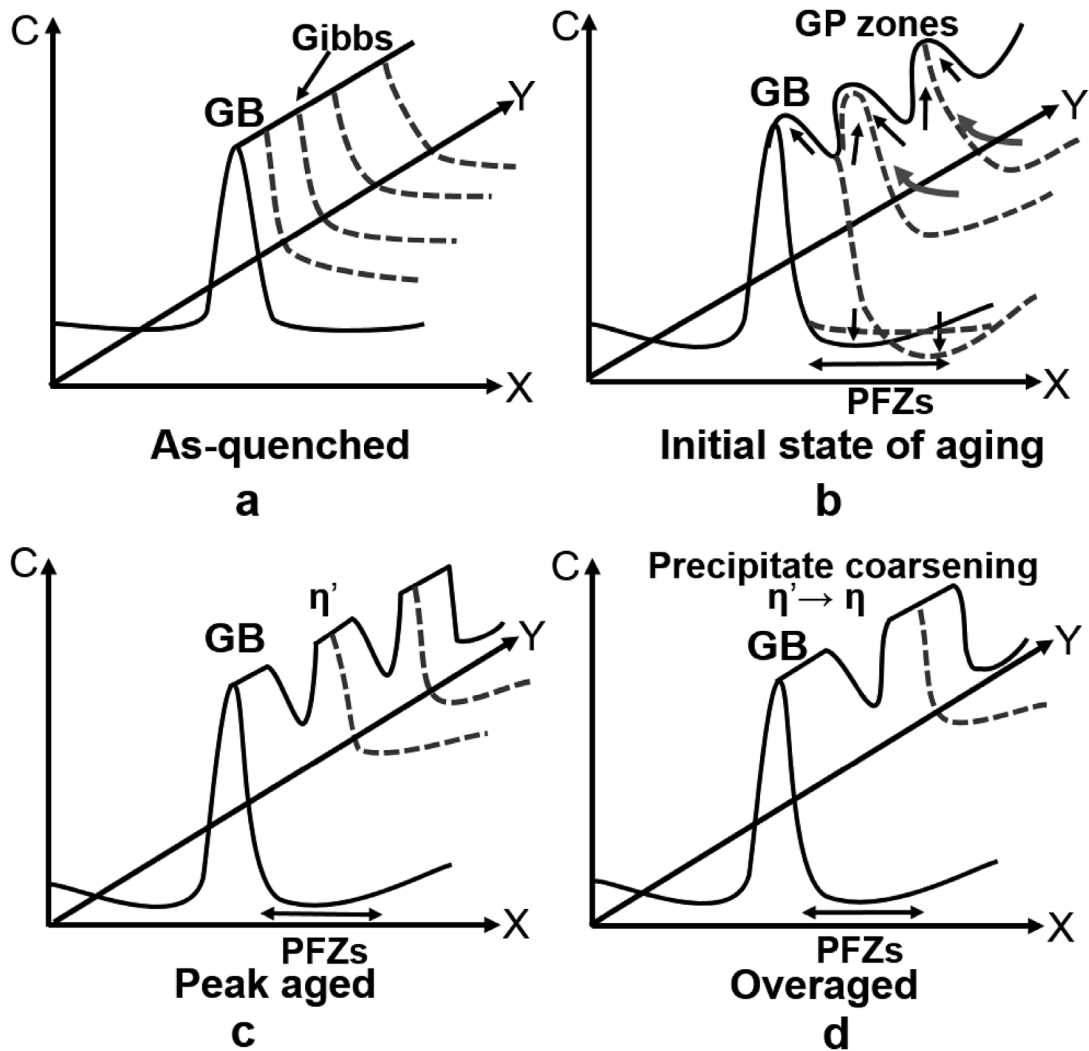


Fig. 11. Schematic diagrams showing the local composition C on a section of grain boundary. Gibbsian segregation and the associated fluctuations allow earlier phase formation during aging on the solute decorated grain boundaries compared to the grain interiors: (a) Gibbsian segregation in the as-quenched state; (b) Compositional grain boundary fluctuations in the initial state of aging (0.5 h at 120 °C); (c) η' formation in the peak aged state, supported by preceding compositional grain boundary fluctuations; (d) Grain boundary precipitate coarsening in the overaged state.

boundaries, where the solute content exceeds that in the bulk, the formation and growth of η' phase keeps on trapping solutes from the grain boundaries and from the matrix. This effect further supports growth of the η' phase to a size of around 40 nm in length on and along the grain boundaries compared to an average size of only 6 nm observed in the bulk.

5. Conclusions

Atom probe tomography has been successfully used to study the atomic-scale mechanisms associated with the effects of segregation on grain boundary precipitation and PFZ formation in a model Al–Zn–Mg–Cu alloy during aging. The observations suggest that segregation has an important influence on grain boundary precipitation. The following conclusions are drawn:

1. Solute segregate to the grain boundaries producing a grain boundary excess of about 2 for Zn, 2 for Mg, and 3 for Cu already in the as-quenched state after the preceding solution heat treatment at 475 °C. This means that grain boundary segregation leads to locally higher composition of Zn, Mg and Cu relative to the bulk and also to higher levels and degrees of solute compositional fluctuations on the grain boundaries. This effect promotes earlier formation of GP zones compared to the grain interior already during the initial stage of aging at 120 °C.
2. With increasing aging time (between 2 h and 24 h at 120 °C), solutes from the bulk keep segregating, forming a flux of solutes towards the grain boundaries. The growth and transformation of GP zones on the grain boundaries are accelerated by the solute segregation from the matrix and enhanced solute diffusion along the grain boundaries.
3. Analysis of the ~10 nm wide precipitate-free zones (PFZs) adjacent to the enriched grain boundaries shows that the depletion zone is determined by (i) interface equilibrium segregation; (ii) formation and coarsening of the grain boundary precipitates and (iii) the diffusion range of the solutes in the matrix.
4. The precipitation kinetics, as observed by the volume fraction, size, and number density, are almost identical next to the depletion zone in the bulk and far inside the bulk grain remote from any grain boundary influence. This observation confirms that the regions influenced by the grain boundaries do not extend beyond the PFZs.

Acknowledgements

H. Zhao would like to acknowledge the China Scholarship Council ("State Scholarship Fund", No. 201506050028) for the PhD scholarship granted to support this work. A. Kwiatkowski da Silva is grateful to the Brazilian National Research Council (Conselho Nacional de Pesquisas, CNPQ) for the PhD scholarship through the "Science without Borders" Project (203077/2014–8). U. Tezins and A. Sturm are acknowledged for their support in the use of the atom probe and PFIB facility at MPIE. The authors are grateful for the Max-Planck Society and the BMBF for the funding of the Laplace and the UGSLIT projects respectively.

References

- [1] D. Raabe, M. Herbig, S. Sandlöbes, Y. Li, D. Tytko, M. Kuzmina, D. Ponge, P.P. Choi, Grain boundary segregation engineering in metallic alloys: a pathway to the design of interfaces, *Curr. Opin. Solid State Mater. Sci.* 18 (4) (2014) 253–261.
- [2] T. Frolov, S.V. Divinski, M. Asta, Y. Mishin, Effect of interface phase transformations on diffusion and segregation in high-angle grain boundaries, *Phys. Rev. Lett.* 110 (25) (2013) 255502.
- [3] M. Kuzmina, D. Ponge, D. Raabe, Grain boundary segregation engineering and austenite reversion turn embrittlement into toughness: example of a 9wt.% medium Mn steel, *Acta Mater.* 86 (2015) 182–192.
- [4] M.P. Harmer, The phase behavior of interfaces, *Science* 332 (6026) (2011) 182–183.
- [5] P. Lejcek, Grain boundary segregation in metals, *Springer Mater. Sci.* 136 (2010).
- [6] J. Nie, Y. Zhu, J. Liu, X. Fang, Periodic segregation of solute atoms in fully coherent twin boundaries, *Science* 340 (6135) (2013) 957–960.
- [7] J. Buban, K. Matsunaga, J. Chen, N. Shibata, W. Ching, T. Yamamoto, Y. Ikuhara, Grain boundary strengthening in alumina by rare earth impurities, *Science* 311 (5758) (2006) 212–215.
- [8] G. Duscher, M.F. Chisholm, U. Alber, M. Ruhle, Bismuth-induced embrittlement of copper grain boundaries, *Nat. Mater.* 3 (9) (2004) 621–626.
- [9] J. Luo, H. Cheng, K.M. Asl, C.J. Kiely, M.P. Harmer, The role of a bilayer interfacial phase on liquid metal embrittlement, *Science* 333 (6050) (2011) 1730–1733.
- [10] R.G. Song, W. Dietzel, B.J. Zhang, W.J. Liu, M.K. Tseng, A. Atrens, Stress corrosion cracking and hydrogen embrittlement of an Al–Zn–Mg–Cu alloy, *Acta Mater.* 52 (16) (2004) 4727–4743.
- [11] B.W. Krakauer, D.N. Seidman, Subnanometer scale study of segregation at grain boundaries in an Fe(Si) alloy, *Acta Mater.* 46 (17) (1998) 6145–6161.
- [12] D. Isheim, R.P. Kolli, M.E. Fine, D.N. Seidman, An atom-probe tomographic study of the temporal evolution of the nanostructure of Fe–Cu based high-strength low-carbon steels, *Scripta Mater.* 55 (1) (2006) 35–40.
- [13] D. Raabe, S. Sandlöbes, J. Millán, D. Ponge, H. Assadi, M. Herbig, P.P. Choi, Segregation engineering enables nanoscale martensite to austenite phase transformation at grain boundaries: a pathway to ductile martensite, *Acta Mater.* 61 (16) (2013) 6132–6152.
- [14] A. Kwiatkowski da Silva, G. Inden, A. Kumar, D. Ponge, B. Gault, D. Raabe, Competition between formation of carbides and reversed austenite during tempering of a medium-manganese steel studied by thermodynamic-kinetic simulations and atom probe tomography, *Acta Mater.* 147 (2018) 165–175.
- [15] M. Herbig, D. Raabe, Y. Li, P. Choi, S. Zaeferrer, S. Goto, Atomic-scale quantification of grain boundary segregation in nanocrystalline material, *Phys. Rev. Lett.* 112 (12) (2014) 126103.
- [16] G. Sha, L. Yao, X. Liao, S.P. Ringer, Z. Chao Duan, T.G. Langdon, Segregation of solute elements at grain boundaries in an ultrafine grained Al–Zn–Mg–Cu alloy, *Ultramicroscopy* 111 (6) (2011) 500–505.
- [17] P.V. Liddicoat, X.Z. Liao, Y. Zhao, Y. Zhu, M.Y. Murashkin, E.J. Lavermia, R.Z. Valiev, S.P. Ringer, Nanostructural hierarchy increases the strength of aluminium alloys, *Nat. Commun.* 1 (2010) 63.
- [18] G. Sha, K. Tugcu, X.Z. Liao, P.W. Trimby, M.Y. Murashkin, R.Z. Valiev, S.P. Ringer, Strength, grain refinement and solute nanostructures of an Al–Mg–Si alloy (AA6060) processed by high-pressure torsion, *Acta Mater.* 63 (2014) 169–179.
- [19] Y. Chen, N. Gao, G. Sha, S.P. Ringer, M.J. Starink, Microstructural evolution, strengthening and thermal stability of an ultrafine-grained Al–Cu–Mg alloy, *Acta Mater.* 109 (2016) 202–212.
- [20] X. Sauvage, N. Enikeev, R. Valiev, Y. Nasedkina, M. Murashkin, Atomic-scale analysis of the segregation and precipitation mechanisms in a severely deformed Al–Mg alloy, *Acta Mater.* 72 (2014) 125–136.
- [21] S.P. Knight, N. Birbilis, B.C. Muddle, A.R. Trueman, S.P. Lynch, Correlations between intergranular stress corrosion cracking, grain-boundary microchemistry, and grain-boundary electrochemistry for Al–Zn–Mg–Cu alloys, *Corrosion Sci.* 52 (12) (2010) 4073–4080.
- [22] R.M. Su, Y.D. Qu, R.D. Li, J.H. You, Influence of RRA treatment on the microstructure and stress corrosion cracking behavior of the spray-formed 7075 alloy, *Mater. Sci.* 51 (3) (2015) 372–380.
- [23] A.C.U. Rao, V. Vasu, M. Govindaraju, K.V.S. Srinadh, Stress corrosion cracking behaviour of 7xxx aluminum alloys: a literature review, *Trans. Nonferrous Metals Soc. China* 26 (6) (2016) 1447–1471.
- [24] P. Pao, M. Gao, R. Wei, Environmentally assisted fatigue-crack growth in 7075 and 7050 aluminum alloys, *Scripta Metallurgica* 19 (3) (1985) 265–270.
- [25] A. Joshi, C. Shastri, M. Levy, Effect of heat treatment on solute concentration at grain boundaries in 7075 aluminum alloy, *Metallurgical Transactions A* 12 (6) (1981) 1081–1088.
- [26] R. Viswanadham, T. Sun, J. Green, Grain boundary segregation in Al–Zn–Mg alloys—implications to stress corrosion cracking, *Metall. Mater. Trans.* 11 (1) (1980) 85–89.
- [27] A.K. Vasudevan, R. Doherty, Grain boundary ductile fracture in precipitation hardened aluminum alloys, *Acta Metallurgica* 35 (6) (1987) 1193–1219.
- [28] T. Ogura, S. Hirohara, A. Cerezo, T. Sato, Atom probe tomography of nanoscale microstructures within precipitate free zones in Al–Zn–Mg(–Ag) alloys, *Acta Mater.* 58 (17) (2010) 5714–5723.
- [29] E.A. Starke, The causes and effects of "denuded" or "precipitate-free" zones at grain boundaries in aluminum-base alloys, *JOM (J. Occup. Med.)* 22 (1) (1970) 54–63.
- [30] R.D. Doherty, Diffusive phase transformation in the solid state, *Physical Metallurgy* (1996) 1363–1505 (Fourth, Revised and Enhanced Edition), North-Holland, Oxford.
- [31] J. Embury, R. Nicholson, The nucleation of precipitates: the system Al–Zn–Mg, *Acta Metall.* 13 (4) (1965) 403–417.
- [32] G. Lorimer, R. Nicholson, Further results on the nucleation of precipitates in the Al–Zn–Mg system, *Acta Metall.* 14 (8) (1966) 1009–1013.

- [33] T. Ogura, A. Hirose, T. Sato, Effect of PFZ and grain boundary precipitate on mechanical properties and fracture morphologies in Al-Zn-Mg(Ag) alloys, *Mater. Sci. Forum* 638–642 (2010) 297–302.
- [34] T. Kawabata, O. Izumi, Ductile fracture in the interior of precipitate free zone in an Al-6.0% Zn-2.6% Mg alloy, *Acta Metall.* 24 (9) (1976) 817–825.
- [35] J. Park, A. Ardell, Microchemical analysis of precipitate free zones in 7075-Al in the T6, T7 and RRA tempers, *Acta Metall. Mater.* 39 (4) (1991) 591–598.
- [36] H. Löffler, I. Kovacs, J. Lendvai, Decomposition processes in Al-Zn-Mg alloys, *J. Mater. Sci.* 18 (8) (1983) 2215–2240.
- [37] G. Sha, A. Cerezo, Early-stage precipitation in Al-Zn-Mg-Cu alloy (7050), *Acta Mater.* 52 (15) (2004) 4503–4516.
- [38] T. Marlaud, A. Deschamps, F. Bley, W. Lefebvre, B. Baroux, Influence of alloy composition and heat treatment on precipitate composition in Al-Zn-Mg-Cu alloys, *Acta Mater.* 58 (1) (2010) 248–260.
- [39] L. Berg, J. Gjønnnes, V. Hansen, X. Li, M. Knutson-Wedel, G. Waterloo, D. Schryvers, L. Wallenberg, GP-zones in Al-Zn-Mg alloys and their role in artificial aging, *Acta Materialia* 49 (17) (2001) 3443–3451.
- [40] S. Ortner, C. Grovenor, B. Shollock, On the structure and composition of GP zones in high purity AlZnMg alloys, *Scripta Metallurgica* 22 (6) (1988) 839–842.
- [41] N.Q. Chinh, J. Lendvai, D.H. Ping, K. Hono, The effect of Cu on mechanical and precipitation properties of Al-Zn-Mg alloys, *J. Alloy. Comp.* 378 (1) (2004) 52–60.
- [42] K. Ma, H. Wen, T. Hu, T.D. Topping, D. Isheim, D.N. Seidman, E.J. Lavernia, J.M. Schoenung, Mechanical behavior and strengthening mechanisms in ultrafine grain precipitation-strengthened aluminum alloy, *Acta Mater.* 62 (2014) 141–155.
- [43] G. Sha, Y. Wang, X. Liao, Z. Duan, S. Ringer, T. Langdon, Influence of equal-channel angular pressing on precipitation in an Al-Zn-Mg-Cu alloy, *Acta Mater.* 57 (10) (2009) 3123–3132.
- [44] M.-h. Li, Y.-q. Yang, Z.-q. Feng, B. Huang, X. Luo, J.-h. Lou, J.-g. Ru, Precipitation sequence of η phase along low-angle grain boundaries in Al-Zn-Mg-Cu alloy during artificial aging, *Trans. Nonferrous Metals Soc. China* 24 (7) (2014) 2061–2066.
- [45] P.N.T. Unwin, R.B. Nicholson, The nucleation and initial stages of growth of grain boundary precipitates in Al-Zn-Mg and Al-Mg alloys, *Acta Metall.* 17 (11) (1969) 1379–1393.
- [46] E. Butler, P. Swann, In situ observations of the nucleation and initial growth of grain boundary precipitates in an Al-Zn-Mg alloy, *Acta Metall.* 24 (4) (1976) 343–352.
- [47] D. Blavette, A. Bostel, J.M. Sarrau, B. Deconihout, A. Menand, An atom probe for three-dimensional tomography, *Nature* 363 (1993) 432.
- [48] D.N. Seidman, Three-dimensional atom-probe tomography: advances and applications, *Annu. Rev. Mater. Res.* 37 (1) (2007) 127–158.
- [49] B. Gault, X.Y. Cui, M.P. Moody, F. De Geuser, C. Sigli, S.P. Ringer, A. Deschamps, Atom probe microscopy investigation of Mg site occupancy within δ' precipitates in an Al-Mg-Li alloy, *Scripta Mater.* 66 (11) (2012) 903–906.
- [50] M.K. Miller, R.G. Forbes, Atom probe tomography, *Mater. Char.* 60 (6) (2009) 461–469.
- [51] L. Reich, M. Murayama, K. Hono, Evolution of Ω phase in an Al-Cu-Mg-Ag alloy—a three-dimensional atom probe study, *Acta Mater.* 46 (17) (1998) 6053–6062.
- [52] S.K. Marya, G. Wyon, Temporary embrittlement followed by increase in ductility after gallium penetration in cold rolled aluminium, *Scripta Metall.* 9 (10) (1975) 1009–1016.
- [53] K.A. Unocic, M.J. Mills, G.S. Daehn, Effect of gallium focused ion beam milling on preparation of aluminium thin foils, *J. Microsc.* 240 (3) (2010) 227–238.
- [54] B. Benson, R. Hoagland, Crack growth behavior of a high strength aluminum alloy during LME by gallium, *Scripta Metallurgica* 23 (11) (1989) 1943–1948.
- [55] Y. Xiao, J. Wehrs, H. Ma, T. Al-Samman, S. Korte-Kerzel, M. Göken, J. Michler, R. Spolenak, J.M. Wheeler, Investigation of the deformation behavior of aluminum micropillars produced by focused ion beam machining using Ga and Xe ions, *Scripta Mater.* 127 (2017) 191–194.
- [56] H. Zhao, B. Gault, D. Ponge, D. Raabe, F. De Geuser, Parameter free quantitative analysis of atom probe data by correlation functions: application to the precipitation in Al-Zn-Mg-Cu, *Scripta Mater.* 154 (2018) 106–110.
- [57] K. Thompson, D. Lawrence, D.J. Larson, J.D. Olson, T.F. Kelly, B. Gorman, In situ site-specific specimen preparation for atom probe tomography, *Ultra-microscopy* 107 (2–3) (2007) 131–139.
- [58] S. Ringer, K. Hono, Microstructural evolution and age hardening in aluminium alloys: atom probe field-ion microscopy and transmission electron microscopy studies, *Mater. Char.* 44 (1–2) (2000) 101–131.
- [60] P.V. Liddicoat, T. Honma, L.T. Stephenson, S.P. Ringer, Evolution of nanostructure during the early stages of ageing in Al-Zn-Mg-Cu alloys, *Mater. Sci. Forum* 519–521 (2006) 555–560.
- [61] T. Engdahl, V. Hansen, P. Warren, K. Stiller, Investigation of fine scale precipitates in Al-Zn-Mg alloys after various heat treatments, *Materials Science and Engineering: A* 327 (1) (2002) 59–64.
- [62] C. Wolverton, Crystal structure and stability of complex precipitate phases in Al-Cu-Mg-(Si) and Al-Zn-Mg alloys, *Acta Mater.* 49 (16) (2001) 3129–3142.
- [63] K. Hono, N. Sano, T. Sakurai, Quantitative atom-probe analysis of some aluminum alloys, *Surf. Sci.* 266 (1–3) (1992) 350–357.
- [64] B. Cai, B. Adams, T. Nelson, Relation between precipitate-free zone width and grain boundary type in 7075-T7 Al alloy, *Acta Mater.* 55 (5) (2007) 1543–1553.
- [65] M. Dumont, W. Lefebvre, B. Doisneau-Cottignies, A. Deschamps, Characterisation of the composition and volume fraction of η' and η precipitates in an Al-Zn-Mg alloy by a combination of atom probe, small-angle X-ray scattering and transmission electron microscopy, *Acta Mater.* 53 (10) (2005) 2881–2892.
- [66] F. De Geuser, W. Lefebvre, Determination of matrix composition based on solute-solute nearest-neighbor distances in atom probe tomography, *Microsc. Res. Tech.* 74 (3) (2011) 257–263.
- [67] B. Gault, F. Danoix, K. Houmada, D. Mangelinck, H. Leitner, Impact of directional walk on atom probe microanalysis, *Ultramicroscopy* 113 (2012) 182–191.
- [68] T. Marlaud, A. Deschamps, F. Bley, W. Lefebvre, B. Baroux, Evolution of precipitate microstructures during the retrogression and re-ageing heat treatment of an Al-Zn-Mg-Cu alloy, *Acta Mater.* 58 (14) (2010) 4814–4826.
- [69] J. Gibbs, *The Collected Works of J. Willard Gibbs*, vol. 1, Yale University Press, New Haven, CT, 1948.
- [70] D. McLean, *Grain Boundaries in Metals*, Oxford University Press, London, 1957.
- [71] M. Seah, E. Hondros, Grain boundary segregation, *Proc. R. Soc. Lond. A* 335 (1601) (1973) 191–212.
- [72] A. Kwiatkowski da Silva, D. Ponge, Z. Peng, G. Inden, Y. Lu, A. Breen, B. Gault, D. Raabe, Phase nucleation through confined spinodal fluctuations at crystal defects evidenced in Fe-Mn alloys, *Nat. Commun.* 9 (1) (2018) 1137.
- [73] P. Unwin, G. Lorimer, R. Nicholson, The origin of the grain boundary precipitate free zone, *Acta Metall.* 17 (11) (1969) 1363–1377.
- [74] P.A. Rometsch, Y. Zhang, S. Knight, Heat treatment of 7xxx series aluminium alloys—some recent developments, *Trans. Nonferrous Metals Soc. China* 24 (7) (2014) 2003–2017.
- [75] T. Ogura, S. Hirose, T. Sato, Quantitative characterization of precipitate free zones in Al-Zn-Mg(-Ag) alloys by microchemical analysis and nano-indentation measurement, *Sci. Technol. Adv. Mater.* 5 (4) (2016) 491–496.